Plasma Phys. Control. Fusion **51** (2009) 124035 (8pp) doi:10.1088/0741-3335/51/12/124035

Fast-electron transport in cylindrically laser-compressed matter

F Perez[1], M Koenig[1], D Batani[2], S D Baton[1], F N Beg[3], C Benedetti[4], E Brambrink[1], S Chawla[3], F Dorchies[5], C Fourment[5], M Galimberti[6], L A Gizzi[7], R Heathcote[6], D P Higginson[3], S Hulin[5], R Jafer[2], P Koester[7], L Labate[7], K Lancaster[6], A J MacKinnon[8], A G McPhee[8], W Nazarov[9], P Nicolai[5], J Pasley[10,6], A Ravasio[1], M Richetta[11], J J Santos[5], A Sgattoni[4], C Spindloe[6], B Vauzour[5] and L Volpe[2]

[1] Laboratoire pour l'Utilisation des Lasers Intenses, Palaiseau, France
[2] Dipartimento di Fisica, Universitˆ di Milano-Bicocca, Italy
[3] University of California, San Diego, La Jolla, USA
[4] Dipartimento di Fisica, Università di Bologna, Italy
[5] Université de Bordeaux - CNRS - CEA, Centre Lasers Intenses et Applications, Talence, F-33405, France
[6] Central Laser Facility, Rutherford Appleton Laboratory, Didcot, UK
[7] LIL-IPCF, Consiglio Nazionale delle Ricerche, PISA, Italy
[8] Lawrence Livermore National Laboratory, USA
[9] University of St Andrews, Fife KY16 9AJ, Scotland
[10] Department of Physics, University of York, YO10 5DD, UK
[11] Dipartimento di Ingegneria Meccanica, Università di Roma Tor Vergata, Italy

Received 30 June 2009, in final form 18 September 2009
Published 11 November 2009
Online at stacks.iop.org/PPCF/51/124035

Abstract

Experimental and theoretical results of relativistic electron transport in cylindrically compressed matter are presented. This experiment, which is a part of the HiPER roadmap, was achieved on the VULCAN laser facility (UK) using four long pulses beams ($\sim 4 \times 50$ J, 1 ns, at 0.53 μm) to compress a hollow plastic cylinder filled with plastic foam of three different densities (0.1, 0.3 and 1 g cm^{-3}). 2D simulations predict a density of 2–5 g cm^{-3} and a plasma temperature up to 100 eV at maximum compression. A short pulse (10 ps, 160 J) beam generated fast electrons that propagate through the compressed matter by irradiating a nickel foil at an intensity of 5×10^{18} W cm^{-2}. X-ray spectrometer and imagers were implemented in order to estimate the compressed plasma conditions and to infer the hot electron characteristics. Results are discussed and compared with simulations.

(Some figures in this article are in colour only in the electronic version)

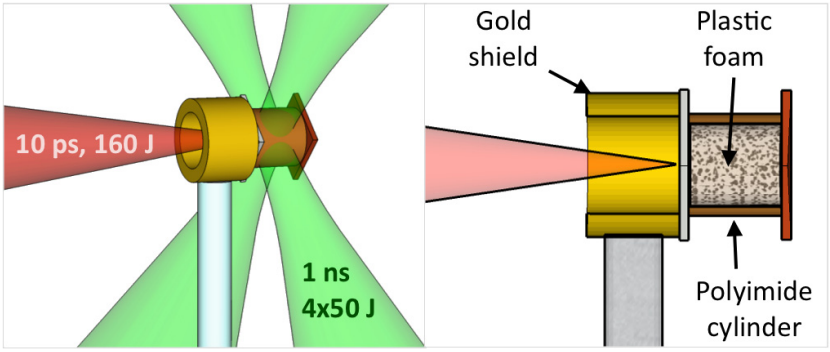

Figure 1. Schematics of the target and lasers design.

1. Introduction

The fast-ignition approach to the inertial confinement fusion scheme requires an improved knowledge of the fast-electron transport inside warm and dense matter [1]. Until now, most of the experiments carried out on this subject were designed to study cold planar targets at solid density. Such low-density and/or cold targets may exhibit a different behaviour of the hot electrons passing through it, compared with the final design. In particular, the stopping power of fast electrons should be affected by the return current, linked to the collective effects. In order to get closer to this goal, we have performed an experiment to study the electron transport in cylindrically compressed matter, which is a useful geometry to infer different measurements [2]. This experiment was split into two parts: the first one to achieve and study the cylindrical compression and the second one to obtain measurements on the electron transport inside this dense matter. This study is one of the key objectives within the HiPER roadmap.

2. Experimental setup

The experiment has been performed on the VULCAN laser facility (UK). Four long-pulse laser beams (about 4×50 to 4×70 J in 1 ns) at 0.53 μm, focused to 150 μm FWHM spots through *hybrid* phase plates, were used to cylindrically compress a 200 μm long polyimide tube. This tube had a 220 μm outer diameter and a 20 μm wall thickness, as shown in figure 1. The target was filled with plastic polymer (TMPTA) at different densities: 0.1 or 0.3 g cm^{-3} foam or 1 g cm^{-3} solid plastic. Both sides were closed with 20 μm thick foils of Ni and Cu, respectively. To produce the hot electrons, an additional laser (160 J in 10 ps) was focused on the Ni layer at an intensity of $\sim 5 \times 10^{18}$ W cm^{-2}, using a $f/3$ off-axis parabola. In order to limit the alteration of the picosecond beam caused by the low-density plasma generated by the nanosecond pulses, a tube-shaped gold shield was stuck on the Ni foil.

The four nanosecond beams had been individually timed to hit the target with a precision better than 100 ps. The delay τ between the long pulses and the short pulse was adjustable from 0 to more than 3 ns with a jitter of ± 100 ps. At $\tau = 0$, the short pulse hit the target when the long pulses just arrived.

The experiment was split into two phases. The first phase objective was to determine the hydrodynamic characteristics of the compressed matter, i.e. its temperature and density at optimal compression. In order to determine some of the parameters of the compressed

cylinder, an additional laser (100 J in 1 ps, 20 μm FWHM) was focused on 10 mm distant foils to make an x-ray or proton backlighter for the diagnostics. Transverse point-projection proton radiography [3] can be employed to infer the target density in shock-compressed targets. A proton source was produced by the short pulse beam focused on gold foils, placed 10 mm away from the target. The detector was a radiochromic film (RCF) stack protected by a 12 μm thick Al foil, placed ∼50 mm away from the target. The stacks were composed of 5 HD and 10 MD 1'×'1 RCFs. Density measurement was also planned with an x-ray radiography diagnostic [4]. Using Ti foils 10 mm away from the target as backlighters and a quartz crystal to reflect the Ti-K_α radiation (at 4.5 keV) that passed through the compressed target, we obtained a magnification of ∼10. In order to get sufficient absorption, the plastic foam was doped with 30% Cl in mass. The quartz crystal (interatomic distance of 1.374 Å) was spherically bent with a radius of curvature 380 mm. Imaging plates positioned ∼2 m away from this crystal detected the Ti-K_α radiation.

The second phase of the experiment was designed to measure the hot electron propagation through the compressed matter. The plastic foam inside the cylinder was doped with 10–20% Cu in mass so as to get x-ray emission from this region. Two spherically bent quartz crystals with a 1.541 Å interatomic distance and a radius of curvature of 380 mm, provided 2D monochromatic images, using imaging plates as detector, around the Cu-$K_{\alpha 1}$ line, i.e. at 8050 ± 5 eV. These crystals were placed to have both side- and rear-view images of the cylinder with a magnification of ∼10 and a spatial resolution between 10 and 20 μm. A cylindrically bent quartz with a 1.012 Å interatomic distance and a radius of curvature of 100 mm, produced time- and space-integrated spectra for x-ray energies from 7.3 to 9.3 keV in a Von Hamos configuration. It was able to detect both the Cu-K_α and Ni-K_α lines with a spectral resolution of 3 ± 2 eV. A second spectrometer consisting of planar highly oriented pyrolitic graphite (HOPG) monitored the same emission lines with a much higher sensitivity [5], but a lower spectral resolution (∼50 eV).

3. Hydrodynamic simulations

Two-dimensional hydrodynamic simulations have been carried out in order to predict the maximum compression achievable. The simulations of the plasma dynamics were performed with the laser–plasma interaction radiation hydrodynamic code CHIC [6, 7].

The code includes two-dimensional axially symmetric hydrodynamics, ion and classical or non-local electron heat conduction, thermal coupling of electrons and ions and a detailed radiation transport. The arbitrary Lagrangian–Eulerian (ALE) method [8] is implemented to improve the geometrical quality of the grid elements and to optimize accuracy robustness, and the computational efficiency [9]. The ionization and the opacity data are tabulated, assuming a local thermodynamic equilibrium (LTE) or a non-LTE depending on the plasma parameters. The radiative transport is computed assuming that the radiation field is quasistationary and weakly anisotropic (multigroup diffusion). The equations of state implemented in the code (QEOS) are described in [10]. The laser propagation, refraction and collisional absorption are treated by a ray tracing algorithm. A resistive MHD package accounting for the azimuthal magnetic fields generated by the thermal sources (crossed gradients of the density and the temperature) is also included.

The cylindrical compression was simulated for the different targets used, and with different laser energies i.e. 4 × 40 J, 4 × 48 J and 4 × 70 J. The absorbed energy varies from 79% in the first case to 73% in the last case. The two examples in figures 2(*a*) and (*b*) correspond to the maximum compression for 0.1 and 1 g cm^{-3} initial targets, respectively, with 4 × 48 J of laser energy. Those two density profiles show a clear difference in the shape of the target: the

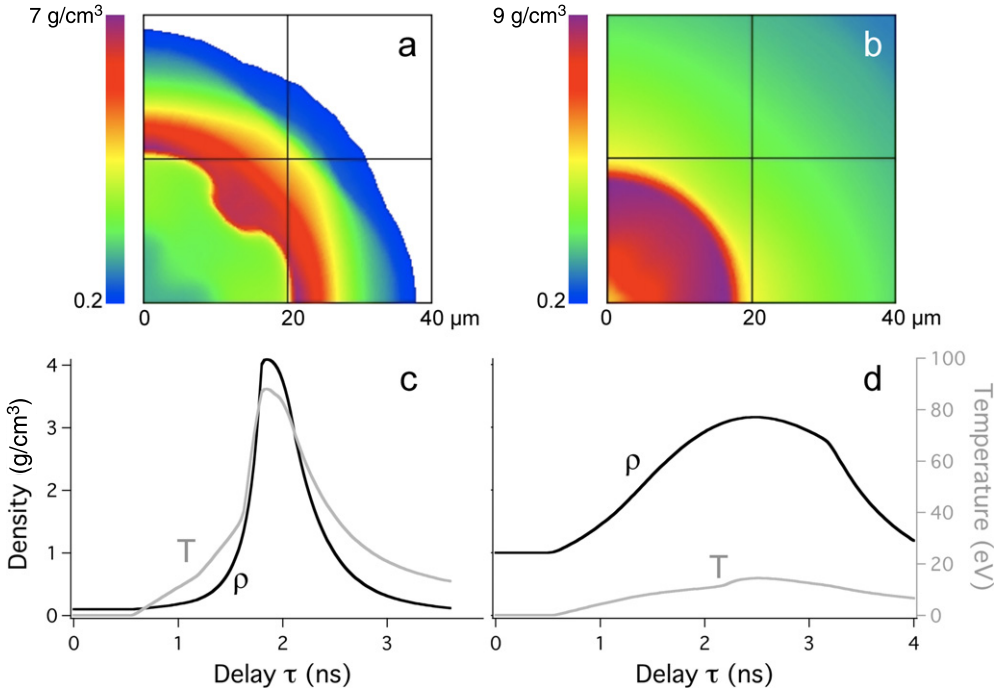

Figure 2. Simulation results for 4 × 48 J of laser energy. (*a*), (*b*) 2D density maps at maximum compression and (*c*), (*d*) evolution of the *volumic mean* density and temperature (mean taken over the core region, which is defined as the plasma originally 180 μm in diameter) for different initial core densities, i.e. 0.1 g cm^{-3} for (*a*), (*c*) and 1 g cm^{-3} for (*b*), (*d*).

0.1 g cm^{-3} case exhibits a dense cylindrical shell containing lower density plasma. The density and temperature evolutions are plotted in figure 2(*c*) and (*d*). One can see that a higher peak density in the centre is achieved with 1 g cm^{-3}, but the temperature is then ∼15 eV, whereas it is about 100 eV with 0.1 g cm^{-3}.

4. Experimental results

In the first phase of the experiment, proton and x-ray radiography were implemented to infer the density of the compressed foam.

Proton radiography examples are shown in figures 3(*a*), (*b*). The difference between the reference shot (without compression) and the others shows that there is a noticeable compression. The limited proton energy we obtained (<10 MeV) induced a limited resolution of the images because of the resulting scattering of the protons. Furthermore, the first RCFs in the stack collect both the protons that were created with a low energy and the ones that were created with a high energy but slowed down while passing through the plasma. Thus, the protons passing early through the target get mixed with the late ones, giving a decreased temporal resolution. This effect also affects the spatial resolution as the target size evolves with time. In order to take all these effects into account, a Monte Carlo code simulated the proton trajectories inside the plasma. This code is a modified version of the PROPEL code [11] developed at LULI. Fixed 2D density maps of the compressed cylinder were taken from the hydrodynamic simulations. The outgoing protons gave a resulting profile of the cylinder on

Figure 3. Proton radiography images of the compressed cylinder (*a*) without compression and (*b*) with compression at $\tau = 1.2$ ns, and a 0.1 g cm^{-3} initial plastic foam inside the cylinder. (*c*) Experimental (dark solid line) and simulated (dotted line) example profiles. The grey line is the corresponding density profile. The cylinder is initially filled with 0.1 g cm^{-3} plastic foam for all these cases.

the different RCFs that was compared with the experimental profiles. An example is shown in figure 3(*c*). The experimental results and simulations are in good agreement. One can also note that the presented diameters of ∼150 μm are well above the theoretical diameters of the cylinder core (∼50 μm). This is due to the low energy of the protons: they cannot penetrate into the core, so we obtain an image of a large low-density plasma. Further analysis is going to be carried out in order to extract more information on these data.

X-ray radiography had the advantage of being able to probe higher plasma densities. The core diameter was more accurately measured thanks to a 30% Cl doping in mass. Examples are shown in figures 4(*a*) and (*b*). In order to compare with the hydrodynamic code results, x-ray absorption simulations through 2D density map has been carried out. An example is shown in figure 4(*c*), where the simulated density and transmission are plotted along a radial direction. It shows that the measurement of FWHM is a good estimation of the core diameter. Thus, both experimental and simulated results are compared in figure 4(*d*). The little number of shots in the 0.1 g cm^{-3} case makes any conclusion difficult, but the good agreement for 1 g cm^{-3} core targets indicates an efficient compression, as predicted by the hydrodynamic simulations. This shows that the hydrodynamic simulations are reliable. Thus, the density and temperature of the compressed target previously calculated can be used to analyse the second phase results.

In this second phase, the two x-ray spectrometers detected the K_α and K_β emission from both Cu and Ni foils. The Ni emission is a good indicator of the electron source. The Cu signal indicates an electron population propagating through the target. The first interesting data are then the ratio between the Cu and Ni signal as it indicates the fraction of the hot (>8 keV) electrons that reached the rear surface of the target. These data are presented in figure 5 for different delays, given by the HOPG spectrometer. There is a clear decrease up to $\tau \sim 2$ ns, after which the ratio is constant. Furthermore, this effect is identical for the three different initial core densities used. These results, discussed below, are validated by the other spectrometer as well as the two x-ray imagers.

The side-view x-ray imager produced images of the Cu-K_α emission from the rear Cu foil, and from the Cu doping inside the plastic core. In the four images of figure 6, the emission from the core is clearly differentiated from the Cu foil one. The vertical size of this core is about 50 μm at maximum compression, which is in agreement with the presented simulations. One can also easily see that the horizontal length of the emitting region inside the cylinder decreases with the delay: the penetration depth of the electrons is reduced for a high compression. For the low-density targets, the number of Cu atoms in the foam turned out to be too low to have a significant number of photons coming out of the target.

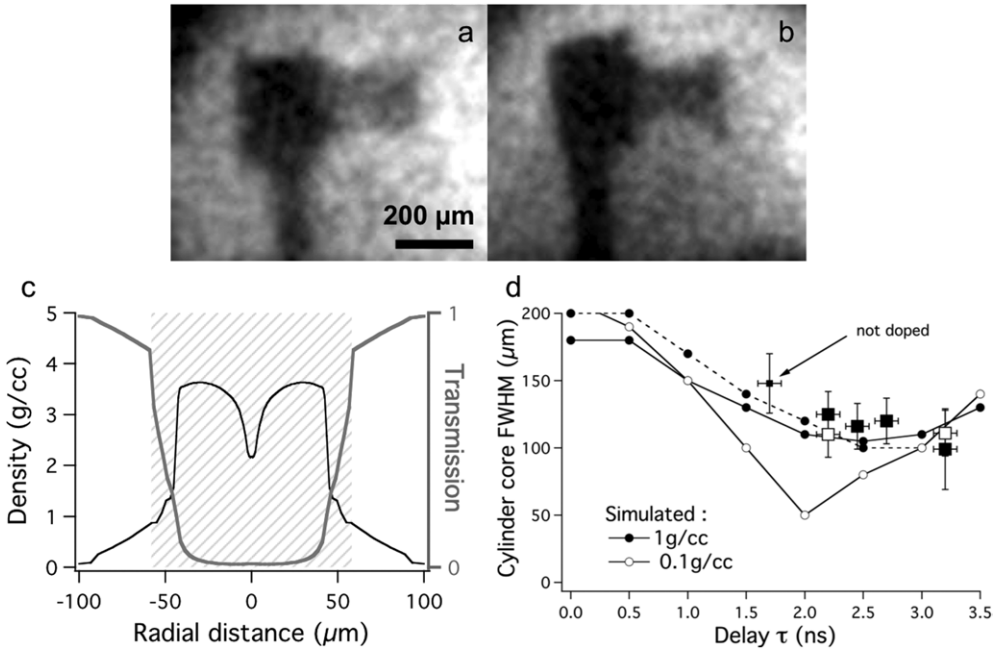

Figure 4. X-ray radiography images of the compressed cylinder (*a*) 500 ps before maximum compression and (*b*) at maximum compression ($\tau = 2.2$ ns). Both these results correspond to a 1 g cm^{-3} initial foam density inside the cylinder. (*c*) Example of simulated density and x-ray transmission radial profiles, with a 30% Cl-doped 1 g cm^{-3} core at $\tau = 3$ ns. The hatched area corresponds to the Cl-doped core. (*d*) Overall results of the x-ray radiography diagnostic. Squares are experimental points and dots are simulated ones. Open or solid points correspond to 0.1 or 1 g cm^{-3}, respectively. Simulation for doping-free core is plotted as a dashed line.

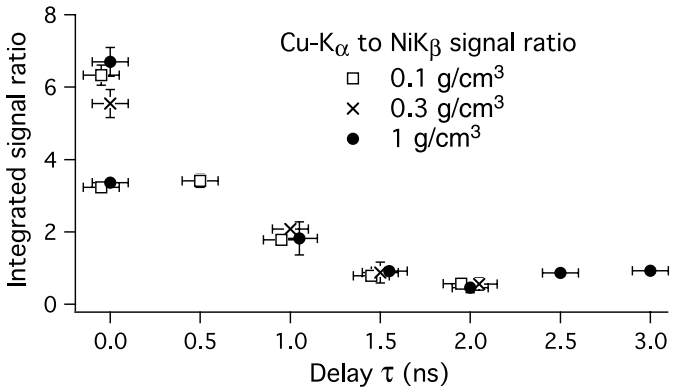

Figure 5. Ratio between Cu and Ni x-ray emissions as measured with the HOPG spectrometer versus the delay τ, for different initial core densities.

Now taking into account the rear Cu foil instead of the core, the measurement of the width of this rear surface Cu-K$_\alpha$ emission is closely linked to the divergence of the electrons reaching the rear surface. The side-view x-ray imager corresponding results are plotted in figure 7. It shows two different behaviours of the hot electron divergence. With low-density targets, the width decreases with the delay. The opposite trend is observed for high-density targets.

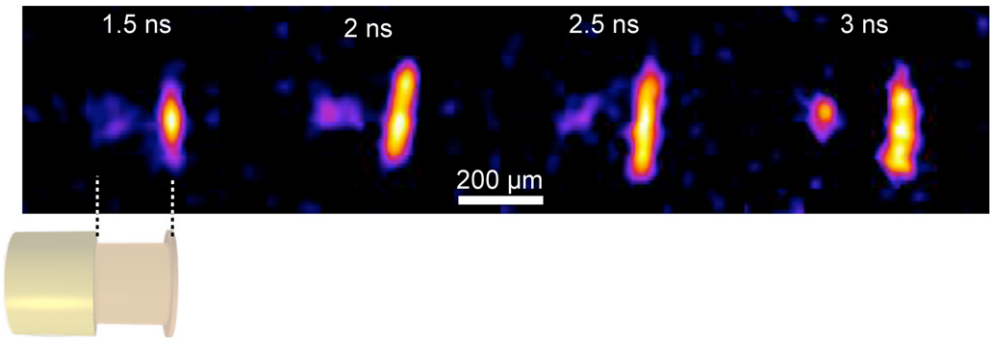

Figure 6. Side-view x-ray images of the Cu-K_α emission from the compressed cylinder at different delays (1 g cm^{-3} initial density in all cases).

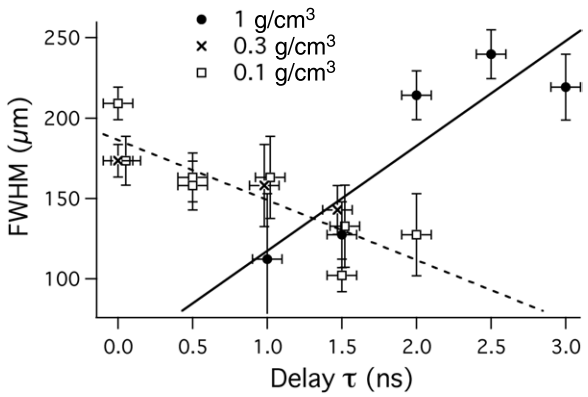

Figure 7. Side-view imager results for fast-electron beam divergence measurements: rear surface foil width for different target densities. Linear fits are plotted for low- or high-density targets.

5. Discussion and conclusion

The second phase results indicate a decreasing fraction of electrons reaching the rear surface when the compression occurs. It shows that the electrons are slowed down more efficiently with a high compression. For delays above 2 ns, the signal shows a plateau which hints at the presence of a hot electron component reaching the rear surface through the high-density core. This is supported by the side-view images of figure 6 as the same integrated signal is always visible on this rear surface. These images also confirm the presence of hot electrons inside the dense target.

To explain the electron divergence behaviour of figure 7, a few leads have to be investigated. We observe two different trends: the spot size either decreases or increases with the compression evolution. For the former case, we can formulate the following explanations. Firstly, the increasing density prevents the coldest electrons from reaching the rear surface. The remaining electrons, being more energetic, are less deviated through the plasma, resulting in a lower detected divergence. Secondly, the low-density targets are composed of a shell that is much denser than the core, as shown in figures 2(*a*) and (*b*). The corresponding density ratio is about 5 : 1 at maximum compression, with a 50 μm diameter core. A resistivity model from [12] and the results from [13] applied to the present case could indicate a resistive confinement of

the electrons inside the cylinder core, thus reducing the electron beam size while the cylinder is being compressed. Similarly, collisional processes might be able to prevent the electrons from diverging through the dense shell. Lastly, the electron beam can be truncated by this shell (because of an increased stopping power) thus giving a smaller spot on the rear surface. All these guiding effects may not apply in the case of high-density (solid) targets. However, it is difficult to say whether they are able to reverse the trend, i.e. divergence increasing with the delay. Indeed, measurements on such a small scale target make their interpretation difficult. To answer this question, electron transport simulations are under consideration.

In conclusion, cylindrical compression has been achieved and measured to be in good agreement with the hydrodynamic simulations, and electron transport features have been measured. Within the fast-ignition framework, the presented results indicate that the same number of fast electrons able to reach the high-density region are observed for different initial target densities. More surprisingly, the electron divergence appears to depend strongly on the plasma geometries achieved for those different initial densities. In order to understand the above results, electron propagation simulations using electron transport codes still need to be performed. As one of the few experiments on electron transport in compressed matter [14], further studies need to be achieved to complete the HiPER roadmap. Overall, this experiment was an important testbed for the lasers and diagnostics in such a new configuration, several challenging experimental points have been clarified and fast-electron behaviours in compressed matter have been underlined.

Acknowledgment

The HiPER project is acknowledged for fully supporting this experiment.

References

[1] Tabak M *et al* 1994 *Phys. Plasmas* **1** 1626–34
[2] Nakamura H *et al* 2008 *Phys. Rev. Lett.* **100** 165001
[3] Le Pape S *et al* 2006 *High Energy Density Phys.* **2** 1–6
[4] Benuzzi-Mounaix A *et al* 2008 *Phys. Rev.* E **77** 045402
[5] Pak A *et al* 2004 *Rev. Sci. Instrum.* **75** 3747–9
[6] Maire P *et al* 2007 *SIAM J. Sci. Comput.* **29** 1781
[7] Maire P and Breil J 2008 *Int. J. Numer. Methods Fluids* **56** 1417–23
[8] Hirt C W *et al* 1997 *J. Comput. Phys.* **135** 203–16
[9] Maire P *et al* 2008 *Int. J. Numer. Methods Fluids* **56** 1161–6
[10] More R M *et al* 1988 *Phys. Fluids* **31** 3059–78
[11] Gremillet L 2001 *PhD Thesis* Ecole Polytechnique
[12] Lee Y T and More R M 1984 *Phys. Fluids* **27** 1273–86
[13] Kar S *et al* 2009 *Phys. Rev. Lett.* **102** 055001
[14] Hall T A *et al* 1998 *Phys. Rev. Lett.* **81** 1003